Surface contributions to the complex neutron-^{208}Pb mean field between -20 and $+20$ MeV

J.-P. Jeukenne
Institut de Physique B5, University of Liège, B-4000 Liège 1, Belgium

C. H. Johnson
Oak Ridge National Laboratory, Oak Ridge, Tennessee 37831

C. Mahaux
Institut de Physique B5, University of Liège, B-4000 Liège 1, Belgium
(Received 11 July 1988)

Phenomenological analyses of the experimental n-^{208}Pb differential, total, and polarization cross sections with local optical-model potentials indicate that the radial shape of the surface absorption depends upon energy below 10 MeV: The corresponding diffuseness decreases and the radius parameter increases with decreasing neutron energy. Because of the dispersion relation that connects the real and imaginary parts of the mean field, these features imply that the real potential contains a surface component whose radial shape also depends upon energy. This radial shape is calculated numerically for typical parametrizations of the energy dependence of the surface absorption; it turns out to be quite complicated for neutron energies between 0 and 15 MeV. In this domain, the predicted differential cross sections are sensitive to the radial shapes of both the real and imaginary surface components of the mean field even though their volume integrals are exactly the same in all the investigated models. The best agreement with the experimental data is obtained for parametrizations in which the radial shape of the surface absorption depends only weakly upon energy. It is shown that good fits to the experimental data can also be obtained in the framework of models in which the radial shape of the surface absorption is independent of energy but in which the strength of the surface absorption depends upon the orbital angular momentum of the incoming neutron. Tentative physical interpretations of these features are proposed.

I. INTRODUCTION

In the familiar optical model it is assumed that the incoming nucleon moves in a local complex mean field, viz.,

$$\mathcal{M}(r;E)=\mathcal{V}(r;E)+i\mathcal{W}(r;E)\ , \tag{1.1}$$

where E is the bombarding energy. This mean field can be continued towards negative energies, for which $\mathcal{V}(r;E)$ is called the shell-model potential. This unified description of the shell-model and optical-model potentials is not only of formal but also of practical interest. In order to gain reliable information on the energy dependence of the depth and radius of $\mathcal{V}(r;E)$ it is indeed necessary to analyze simultaneously the bound ($E<0$) and scattering ($E>0$) data. Two methods have recently been developed.[1,2] They are both based on the following dispersion relation (DR) which connects the real and imaginary parts of the mean field:

$$\mathcal{V}(r;E)=\mathcal{V}_H(r;E)+\Delta\mathcal{V}(r;E)\ , \tag{1.2}$$

$$\Delta\mathcal{V}(r;E)=\frac{\mathrm{P}}{\pi}\int_{-\infty}^{\infty}\mathcal{W}(r;E')/(E'-E)dE'\ ; \tag{1.3}$$

P denotes a principal value integral.

It is plausible to adopt a Woods-Saxon shape for the Hartree-Fock contribution $\mathcal{V}_H(r;E)$:

$$\mathcal{V}_H(r;E)=V_H(E)f(X_H)\ , \tag{1.4}$$

$$f(X_H)=[1+\exp(X_H)]^{-1}\ , \tag{1.5a}$$

$$X_H=(r-R_H)/a_H,\quad R_H=r_H A^{1/3}\ . \tag{1.5b}$$

In practice one can assume that the shape parameters r_H and a_H are independent of energy and that the depth is an exponential function of energy:[2,3]

$$V_H(E)=V_H(0)\exp(-\alpha E)\ . \tag{1.6}$$

The main interest of the DR is that the complicated energy dependence of $\mathcal{V}(r;E)$ is contained in the dispersive contribution $\Delta\mathcal{V}(r;E)$, which can be calculated from the imaginary part of the mean field. The latter is usually decomposed into volume-shaped and surface-peaked components:

$$\mathcal{W}(r;E)=\mathcal{W}_v(r;E)+\mathcal{W}_s(r;E)\ , \tag{1.7}$$

$$\mathcal{W}_v(r;E)=W_v(E)f(X_v)\ , \tag{1.8}$$

$$\mathcal{W}_s(r;E)=W_s(E)g(X_s)\ , \tag{1.9a}$$

$$g(X_s)=-4a_s\frac{d}{dr}f(X_s)\ . \tag{1.9b}$$

The dispersive contribution is then the sum of volume and surface components:

$$\Delta\mathcal{V}(r;E)=\Delta\mathcal{V}_v(r;E)+\Delta\mathcal{V}_s(r;E)\ , \tag{1.7'}$$

where, for instance,

$$\Delta\mathcal{V}_s(r;E)=\frac{\mathrm{P}}{\pi}\int_{-\infty}^{\infty}\mathcal{W}_s(r;E')/(E'-E)dE'\ . \tag{1.10}$$

In Ref. 2 the experimental n-^{208}Pb scattering data were analyzed in the framework of a mean field model in which the DR was explicitly taken into account within the assumption that the shape parameters r_s and a_s are independent of energy. This analysis yielded good fits to the experimental cross sections for neutron energies larger than 10 MeV, and accurately predicted the observed single-particle energies (-20 MeV $<E<0$). For small positive energies ($0<E<10$ MeV), however, this dispersive optical-model analysis yielded rather poor fits to the differential cross sections.

Two possible ways of improving the agreement between the model and the experimental data at small bombarding energies were suggested in Ref. 2, namely: (i) take into account the fact that phenomenological fits with local optical-model potentials indicate that at low energy the shape parameters r_s and a_s associated with the surface absorption depend upon energy; (ii) introduce the possibility that the strength $W_s(E)$ of the surface absorption depends upon the orbital angular momentum of the incoming nucleon.

The main purpose of the present paper is to properly include these two refinements in the dispersive optical-model analysis. This was done only in an approximate way in Ref. 2. There indeed, the radial shape of $\Delta\mathcal{V}_s(r;E)$ was chosen in a semiphenomenological way rather than calculated from the DR (1.10); the latter was replaced by the following less stringent relation between the volume integrals per nucleon (in short, volume integrals):

$$J_{\Delta\mathcal{V}_s}(E)=\frac{\mathrm{P}}{\pi}\int_{-\infty}^{\infty}J_{\mathcal{W}_s}(E')/(E'-E)dE'\ , \tag{1.11}$$

where

$$J_{\Delta\mathcal{V}_s}(E)=\frac{4\pi}{A}\int_0^{\infty}\Delta\mathcal{V}_s(r;E)r^2dr\ , \tag{1.12a}$$

$$J_{\mathcal{W}_s}(E)=\frac{4\pi}{A}\int_0^{\infty}\mathcal{W}_s(r;E)r^2dr\ . \tag{1.12b}$$

As described in Ref. 2 the volume-shaped components $\mathcal{V}_H(r;E)$, $\mathcal{W}_v(r;E)$, and $\Delta\mathcal{V}_v(r;E)$ are mainly determined by the experimental differential and total cross sections for $E>14$ MeV and by the observed value of the Fermi energy. Accordingly, those components are practically not affected by modifications of the parametrization of $\mathcal{W}_s(r;E)$ for small values of E. Throughout the present work we therefore retain exactly the same values of $\mathcal{V}_H(r;E)$, $\mathcal{W}_v(r;E)$, and $\Delta\mathcal{V}_v(r;E)$ as in Ref. 2. We shall also keep the same spin-orbit coupling, and the same values of $\mathcal{W}_s(r;E)$ for energies larger than 12 MeV. Throughout, as in Ref. 2, we assume that $\mathcal{W}(r;E)$ is symmetric about the Fermi energy, for which we take

$$E_F=-6\ \text{MeV}\ . \tag{1.13}$$

Thus, we modify only the parametrization of $\mathcal{W}_s(r;E)$, and we do that only for values of E smaller than 12 MeV. In order to explore a range of parametrizations we first review the original parametrization from Ref. 2 and then present five modifications. The success of each of these six models is evaluated by comparisons with experimental data at several energies. We judge in two ways. (i) We compare at each energy the predicted and experimental differential scattering cross sections by performing plots of the angular distributions and, more quantitatively, by examining the χ^2/N calculated from the N experimental points. We extend the comparison above 12 MeV because, even though $\mathcal{W}_s(r;E)$ is not modified above 12 MeV, $\Delta\mathcal{V}_s(r;E)$ is changed for $E>12$ MeV since the DR (1.10) involves $\mathcal{W}_s(r;E')$ for all E'. However, we limit this extension to $E<20$ MeV because the modifications of $\Delta\mathcal{V}_s(r;E)$ are negligible at higher energies. (ii) We perform least-squares fits to the experimental data with, as fitted adjustable parameters, renormalization factors for the real and imaginary surface components. This second method provides clues as to how the model might be improved to better describe the experimental data. We extend these searches up to 40 MeV; they take into account the differential and total cross sections and, where available, the polarization data. More importantly, we also extend these searches to negative energies by calculating the renormalization factors by which $\Delta\mathcal{V}_s(r;E_{nlj})$ should be multiplied in order to reproduce the observed energies E_{nlj} of the bound single-particle states (-18 MeV $<E_{nlj}<0$).

This paper is organized as follows. In Sec. II we briefly recall the main results of the analysis performed in Ref. 2, in which the shape parameters r_v, a_v, r_s, and a_s were independent of energy. In Sec. III we first present phenomenological evidence that the shape parameters r_s and a_s of the surface absorption depend on energy for $E<10$ MeV. We adopt two typical parametrizations of this energy dependence and calculate numerically the corresponding dispersive contributions $\Delta\mathcal{V}_s(r;E)$. These turn out to have rather complicated radial shapes, which furthermore strongly depend on energy for $E<14$ MeV. We investigate to what extent these calculated $\Delta\mathcal{V}_s(r;E)$ yield good agreement with the experimental differential and polarization cross sections in the domain $4\le E\le 14$ MeV, and with the observed energies of the bound single-particle states (-18 MeV $<E_{nlj}<0$). Section IV is devoted to models in which the strength $W_s(E)$ of the surface absorption depends upon the orbital angular momentum of the neutron. Three cases are considered in which, respectively, (i) r_s is fixed and a_s strongly depends upon energy; (ii) r_s is fixed and a_s weakly depends upon energy; (iii) r_s and a_s are kept fixed. In Sec. V we explain the origin of the rather complicated radial shapes of the surface dispersive correction $\Delta\mathcal{V}_s(r;E)$ calculated in the models of Secs. III and IV. Finally, Sec. VI contains a summary and discussion.

II. FIXED GEOMETRY

Here we review briefly the "fixed-geometry" model which was studied in Secs. III–V of Ref. 2 and which we denote here by FX. From the viewpoint of the present paper the distinguishing feature of this FX model is that the shape parameters r_s and a_s of the surface absorptions, Eqs. (1.9), are independent of energy; specifically,

$$r_s = 1.27 \text{ fm}, \quad a_s = 0.58 \text{ fm} . \tag{2.1}$$

Then the radial shape of the surface dispersive contribution is also independent of energy:

$$\Delta\mathcal{V}_s(r;E) = \Delta V_s(E) g(X_s) , \tag{2.2a}$$

where

$$\Delta V_s(E) = \frac{\mathrm{P}}{\pi} \int W_s(E')/(E'-E) dE' . \tag{2.2b}$$

The strength $W_s(E)$ is parametrized by contiguous linear segments (see Fig. 3 of Ref. 2 and Fig. 6 below):

$$W_s(E) = -0.4(E - E_F) \text{ for } -6 < E < 10 \text{ MeV} , \tag{2.3a}$$

$$W_s(E) = 0.103(E - 72) \text{ for } 10 < E < 72 \text{ MeV} , \tag{2.3b}$$

$$W_s(E) = 0.0 \text{ for } E > 72 \text{ MeV} ; \tag{2.3c}$$

we recall that $W_s(E)$ is symmetric about $E = -6$ MeV.

In Fig. 1 the solid curves represent the differential cross sections predicted from the FX model for $4 \le E \le 14$ MeV, and the solid points the experimental cross sections. The column labeled FX in Table I lists the associated χ^2/N at each energy, where N is the number of experimental points. It is seen that, for $5.5 < E < 10$ MeV, the model predictions are not very good at large angles, $\vartheta > 100°$.

In the following sections we introduce refinements in order to improve the description of the scattering cross sections for $E < 10$ MeV. Before proceeding to those models, we seek insight by renormalizing the real and imaginary surface potentials for the present FX model in order to better fit the data. In so doing, it is important to examine a broad region of both positive and negative energies because the role of the DR cannot be reliably evaluated from a study of a narrow energy domain. At the positive energies, we multiply the real and imaginary surface components of the FX model by renormalization factors, namely, use the following complex surface component:

$$\lambda_s^{(V)}(E)\Delta\mathcal{V}_s(r;E) + i\lambda_s^{(W)}(E)\mathcal{W}_s(r;E) ; \tag{2.4a}$$

we determine the renormalization factors $\lambda_s^{(V)}(E)$ and $\lambda_s^{(W)}(E)$ by performing least-squares fits to the experimental data for $4 \le E \le 40$ MeV, including total cross sections and the polarization data [as in Ref. 2 a ($\pm 0.1\%$) uncertainty was assigned to the total cross section]. At the negative energies E_{nlj} of the single-particle states, we consider only the real part of the surface potential: we take

$$\lambda_s^{(V)}(E_{nlj})\Delta\mathcal{V}_s(r;E_{nlj}) \tag{2.4b}$$

and we adjust the factors $\lambda_s^{(V)}(E_{nlj})$ to reproduce the observed E_{nlj}.

In Fig. 2 the volume integrals derived from these least-squares fits are represented by dots for $E > 0$ and by crosses for $E < 0$. The linear segments in the upper drawing show the imaginary volume integrals of the FX model; they are obtained by multiplying the right-hand sides of Eqs. (2.3) by the geometric factor (8.09 fm^3) associated with the fixed geometry of Eq. (2.1), viz.,

$$J_{\mathcal{W}_s}(E) = -3.24(E - E_F) \text{ for } -6 < E < 10 \text{ MeV} , \tag{2.5a}$$

$$J_{\mathcal{W}_s}(E) = 0.834(E - 72) \text{ for } 10 < E < 72 \text{ MeV} , \tag{2.5b}$$

$$J_{\mathcal{W}_s}(E) = 0.0 \text{ for } E > 72 \text{ MeV} . \tag{2.5c}$$

The curve in the lower drawing is derived by inserting the parametrization (2.5) in the DR, Eq. (1.11). In fact, except for the geometric factor of 8.09 fm^3, our Fig. 2 is the same as Fig. 3 of Ref. 2; we show it here in order to facilitate the comparison with the refined models that will be considered here.

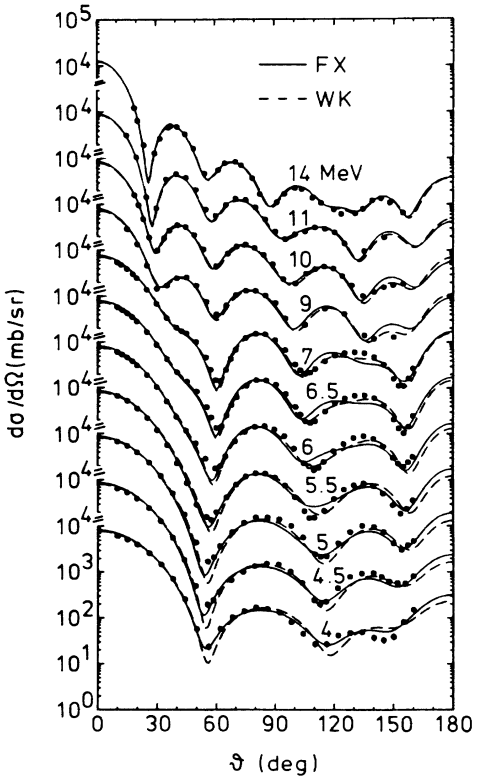

FIG. 1. The dots give the experimental n-^{208}Pb differential cross sections at 7, 9, 10, 11, and 14 MeV and the shape elastic part of the experimental differential cross sections at 4, 4.5, 5, 5.5, 6, and 6.5 MeV; the sources of these data are specified in Ref. 2. The solid curves have been calculated from the FX model (Sec. II). The dashed curves are associated with the WK model (Sec. III C).

TABLE I. χ^2/N from comparisons of model predictions to experimental angular distributions for N scattering angles at the neutron energy E. (i) See Sec. VI of Ref. 2. (ii) See Sec. VII of Ref. 2.

E (MeV)	FX (Sec. II)	SG (Sec. III B)	(i)	WK (Sec. III C)	L-SGa_s (Sec. IV A)	(ii)	L-WKa_s (Sec. IV C)	L-FX (Sec. IV D)
4.0	4.7	16.8	11.5	6.9	8.4	3.2	6.2	13.2
4.5	9.1	12.1	6.6	7.0	7.1	6.4	5.7	10.1
5.0	11.9	13.9	6.2	8.8	9.5	6.4	7.8	11.4
5.5	13.3	47.7	11.8	19.7	22.1	14.6	12.8	7.5
6.0	43.8	37.9	17.6	22.6	32.2	11.6	16.8	19.8
6.5	54.7	41.4	25.2	23.2	47.1	5.5	19.9	22.3
7.0	47.0	34.6	26.6	23.1	34.6	6.9	13.5	20.7
9.0	36.4	17.9	33.6	16.8	31.2	15.6	17.2	20.3
10.0	20.2	16.6	20.2	9.6	28.2	9.0	14.5	8.9
11.0	11.6	16.1	11.7	11.4	15.2	11.4	12.0	11.4
14.0	12.0	14.2	12.0	10.0	18.2	12.0	14.8	13.8

In the lower part of Fig. 2, the crosses at negative energies lie close to the predicted curve. At positive energies, the dots agree well with the predicted curve, except in the region below 10 MeV where the dots lie below the curve; this is the same energy domain in which the angular distributions in Fig. 1 are poorly described by the FX model.

We note that the general good agreement between the points and the curves in Fig. 2 results partly from the parametrization of the FX model adopted in Ref. 2: the linear segments in the upper figure were chosen to give a good description of the points, and the parameters of the Hartree-Fock potential were chosen in part to give good average agreement with the dispersive curve for negative energies and for energies from 14 to 40 MeV.

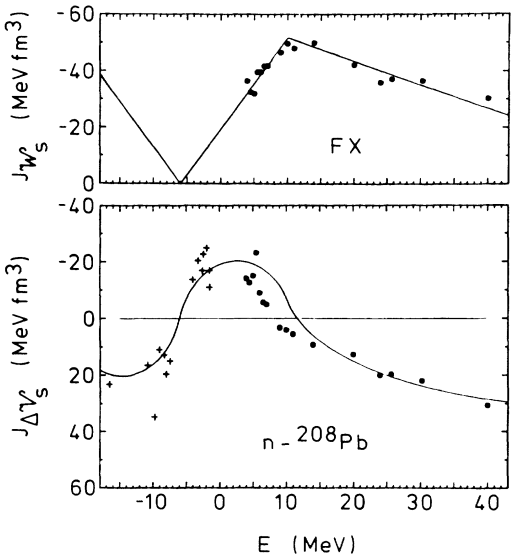

FIG. 2. Energy dependence of the volume integrals per nucleon of the imaginary (top) and real (bottom) components of the mean fields in the case of the FX model of Sec. II. The dots are obtained by multiplying the surface components of the FX model by renormalization factors, expression (2.4a), and by adjusting the latter to a best least-squares fit to the experimental cross section at that energy. The crosses are obtained by multiplying the surface component of the FX model by a renormalization factor, expression (2.4b), and by choosing the latter in such a way that the observed single-particle energies are reproduced.

Within a fixed-geometry model, the authors of Ref. 2 were unable to find a better set of parameters to improve the agreement with the angular distributions below 10 MeV without disturbing the good fits at other energies. One can reasonably conclude that a fixed-geometry model is too restrictive to describe the imaginary potential for $E < 10$ MeV, and that in the lower part of Fig. 2 the deviations of the dots from the dispersive curve in that energy region result because the least-squares searches try to compensate for this inadequacy. Our goal in the following sections is to refine the FX model by allowing more flexibility in the parametrization. However, we reiterate the conclusion from Ref. 2 that the FX model is overall quite successful, considering the small number of adjustable parameters. This success is attributed to the DR. The data would not be described nearly as well if one were to omit the dispersive corrections while adopting a fixed Woods-Saxon geometry for the real part of the potential, as is done in usual "global" optical-model fits.

III. ENERGY-DEPENDENT SURFACE GEOMETRY

A. Phenomenological evidence

Here we consider the same set of phenomenological local optical-model potentials as that described in Sec. 3.3 of Ref. 1, except that we drop the potential at 0.98 MeV where only the total cross section was available and fitted. These potentials are phenomenological in the sense that the DR is not taken into account; they involve up to seven adjusted parameters, which were determined by least-squares fits to experimental differential cross sections. The crosses in Fig. 3 represent the diffuseness parameter a_s associated with the surface absorption of these phenomenological optical-model potentials. They exhibit a clear trend that the diffuseness decreases as the neutron energy falls below 10 MeV; a similar trend has been observed in other cases, in particular ^{89}Y (Ref. 4), ^{59}Co (Ref. 5), ^{209}Bi (Ref. 6), and ^{51}V (Ref. 7). The crosses in Fig. 4

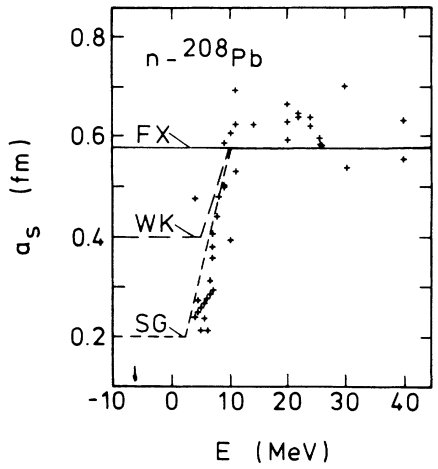

FIG. 3. Diffuseness of the surface absorption [Eqs. (1.9)] of the phenomenological optical-model potentials compiled in Sec. 3.3 of Ref. 1. The horizontal line shows the value $a_s = 0.58$ fm adopted in the FX model, Eq. (2.1). The short-dashed line corresponds to the SG parametrization of Eqs. (3.3). The long-dashed line gives the WK parametrization of Eqs. (3.7).

represent the radius parameter r_s of the surface absorption of these phenomenological optical-model potentials; this radius parameter tends to increase as the neutron energy falls below 10 MeV; the scatter of the empirical values of r_s is fairly large so that this trend is less pronounced than in the case of the diffuseness.

Below, we shall consider two typical parametrizations that take into account the energy dependence of the shape parameters r_s and a_s. In each case we shall choose the strength $W_s(E)$ in such a way that the volume integral $J_{\mathcal{W}_s}(E)$ remains unchanged. Indeed, it is known that the scattering cross sections are sensitive mainly (though not only, see below) to the volume integral of the imaginary and real parts of the optical-model potential. In Secs III B and III C we shall change the shape parameters r_s and a_s from their fixed values of Eq. (2.1); in each case we shall determine the strength $W_s(E)$ in such a way that the volume integral of $\mathcal{W}_s(r;E)$ is given by Eqs. (2.5).

Throughout the present work we adopt the same volume-shaped absorption $\mathcal{W}_v(r;E)$ as in Ref. 2. The reliability of this choice as well as the parametrization of Eqs. (2.5) is illustrated in Fig. 5, which shows that the volume integrals of the phenomenological absorptive potentials compiled in Figs. 3 and 4 are in good agreement with the linear segments which represent the parametrization that had been adopted in Ref. 2 for the volume integral of the full imaginary part, i.e., for the sum

$$J_{\mathcal{W}}(E) = J_{\mathcal{W}_v}(E) + J_{\mathcal{W}_s}(E) \ . \tag{3.1}$$

B. Strong energy dependence of r_s and a_s

In Eqs. (6.4a)–(6.4c) of Ref. 2 it was proposed to parametrize the shape parameters of the surface absorption as follows (in fm):

$$r_s = 1.41 \quad \text{for } E < 2.6 \text{ MeV} \ , \tag{3.2a}$$

$$r_s = 1.41 - 0.0189(E - 2.6) \quad \text{for } 2.6 < E < 10 \text{ MeV} \ , \tag{3.2b}$$

$$r_{s=1.27} \quad \text{for } 10 \text{ MeV} < \text{E} \ , \tag{3.2c}$$

and

$$a_s = 0.20 \quad \text{for } E < 2.6 \text{ MeV} \ , \tag{3.3a}$$

$$a_s = 0.20 + 0.0513(E - 2.6) \quad \text{for } 2.6 < E < 10 \text{ MeV} \ , \tag{3.3b}$$

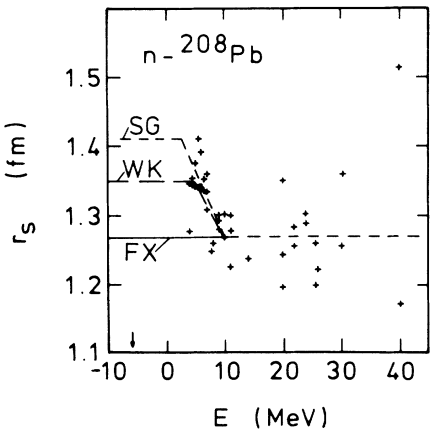

FIG. 4. Radius parameter of the surface absorption [Eqs. (1.9)] of the phenomenological optical-model potentials which belong to the set described in Sec. 3.3 of Ref. 1. The horizontal line shows the value $r_s = 1.27$ fm of the FX model, Eq. (2.1). The short-dashed line corresponds to the SG parametrization of Eqs. (3.2). The long-dashed line gives the WK parametrization of Eqs. (3.7).

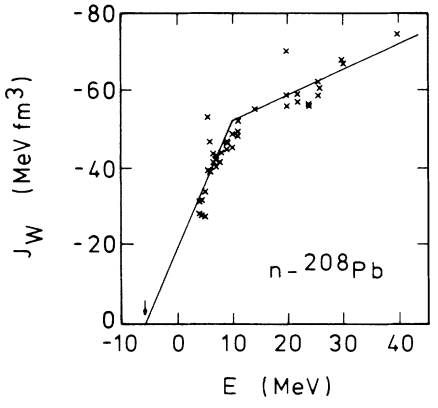

FIG. 5. Energy dependence of the volume integral per nucleon of the full (surface plus volume) absorptive part of the mean field. The crosses correspond to the same phenomenological optical-model potentials as those used in Figs. 3 and 4. The straight lines represent the parametrization which was adopted in the dispersive optical-model analysis of Ref. 2 and which is used throughout the present work.

$$a_s = 0.58 \text{ for } 10 \text{ MeV} < E \ . \tag{3.3c}$$

This parametrization will henceforth be referred to as SG, for "strong" energy dependence of a_s, r_s. The short-dashed lines in Figs. 3 and 4 shows that this SG parametrization of r_s, a_s is in good agreement with the trends which emerge from the available phenomenological optical-model potentials. This is not trivial since originally[2] this SG parametrization was proposed on the basis of fairly specific optical-model fits to the experimental cross sections.

The SG model is specified by the geometric parameters of Eqs. (3.2) and (3.3) and by the requirement that the volume integral of $\mathcal{W}_s(r;E)$ be given by Eqs. (2.5). The corresponding strength $W_s(E)$ is represented by the short-dashed curve in Fig. 6. The dispersive term $\Delta\mathcal{V}_s(r;E)$ is found by numerical evaluation of the integral in Eq. (1.10). As will be demonstrated in Sec. V below, the radial shape of $\Delta\mathcal{V}_s(r;E)$ deviates considerably from the derivative of a Woods-Saxon, in contrast with the assumption made in Sec. VI of Ref. 2.

The differential cross sections predicted by the SG model are represented by the dashed curves in Fig. 7. The symbols represent the same experimental data as in Fig. 1. The associated χ^2/N are contained in the column labeled SG in Table I. Comparisons with the FX model of Sec. II show that the SG model gives slight improvements for $6 \leq E \leq 10$ MeV but poorer agreement with the data for $4 \leq E \leq 5.5$ MeV. For the latter lower energies the predicted minima are too deep and occur at too large angles.

To gain further insight into the SG model we renormalize the surface terms in like manner as in Sec. II: we introduce the SG surface potentials into expressions (2.4a) and (2.4b) and adjust the renormalization factors to best fit the data. In Fig. 8, the crosses and dots represent

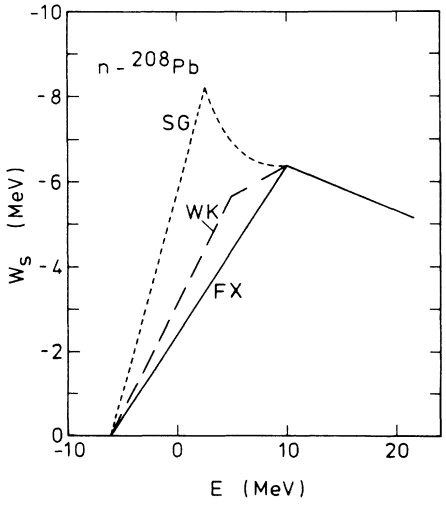

FIG. 6. Energy dependence of the strength of the surface absorption in the FX model of Sec. II (solid lines), in the SG model of Sec. II B (short-dashed line) and in the WK model of Sec. III C (long-dashed line).

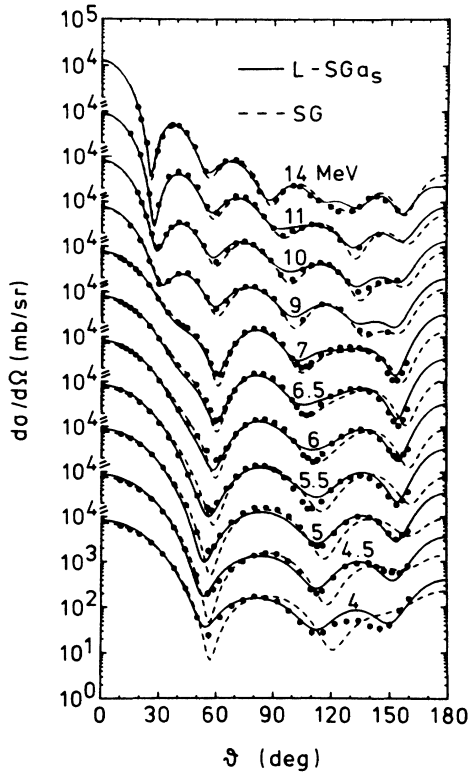

FIG. 7. Angular dependence of the differential n-^{208}Pb cross sections. The dots are the same experimental values as in Fig. 1. The dashed curves give the predictions of the SG model of Sec. III A. The solid curves represent the predictions of the L-SGa_s model of Sec. IV A.

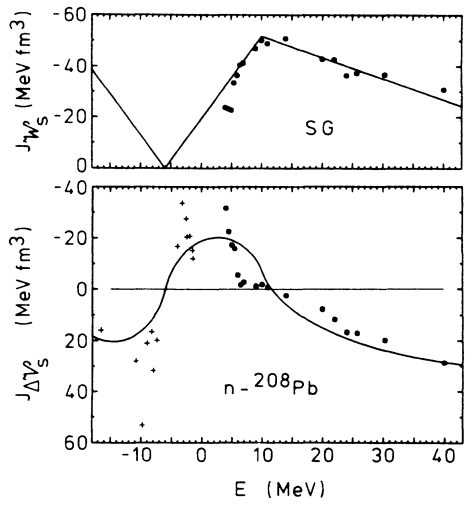

FIG. 8. Energy dependence of the volume integrals per nucleon of the imaginary (top) and real (bottom) components of the mean fields in the case of the SG model of Sec. III B. The dots are obtained by multiplying the surface components of the SG model by renormalization factors, expression (2.4a), and by adjusting the latter to a best least-squares fit to the experimental cross section at that energy. The crosses are obtained by multiplying the surface component of the SG model by a renormalization factor, expression (2.4b), and by choosing the latter in such a way that the observed single-particle energies are reproduced. The model curves are the same as in Fig. 2.

the resulting volume integrals; the curves are the same curves as in Fig. 2. The fact that the dots in the upper part of Fig. 8 follow the linear segments almost as well as in Fig. 2 supports our assumption that the imaginary volume integral is approximately the same for the SG as for the FX model; one might redraw the lower segment with a higher threshold but that would change only slightly the dispersive curve in the lower part of Fig. 8.

The dots and crosses in the lower part of Fig. 8 do not follow the dispersive curve as well as was the case in Fig. 2 for the FX model. In particular, the crosses associated with the bound states tend to lie under the model curve for occupied states (-12 MeV $< E < E_F$) and above it for unoccupied valence states ($E_F < E < 0$). In other words, the absolute value of the strength of the predicted real surface dispersive correction has to be increased in order to reproduce the observed single-particle energies. A likely explanation is the following. Figure 9 shows that near the Fermi energy the radial shape of the calculated real surface component $\Delta\mathcal{V}_s(r;E\approx E_F)$ is approximately given by $g(X_s)$ with $R_s\approx 8.3$ fm, $a_s\approx 0.24$ fm. This real surface dispersive correction is narrow and peaked beyond the average root-mean-square radius of the valence orbits (6.8 fm, see Table V of Ref. 2). In contrast, the surface dispersive correction in the FX model is peaked at $R_s=7.52$ fm and is fairly broad ($a_s=0.58$ fm). Near the Fermi energy, the surface dispersive correction thus has a larger overlap with the bound states' orbits in the FX than in the SG model. The fact that the crosses lie closer to the predicted curve in Fig. 1 than in Fig. 8 therefore probably reflects the feature that the assumed increase of r_s at low energy is too large in the case of the SG model.

Thus, the single-particle energies depend upon the radial shape of the surface component, not just its volume integral. This is also true for the predicted scattering cross sections. This can be exhibited by comparing the

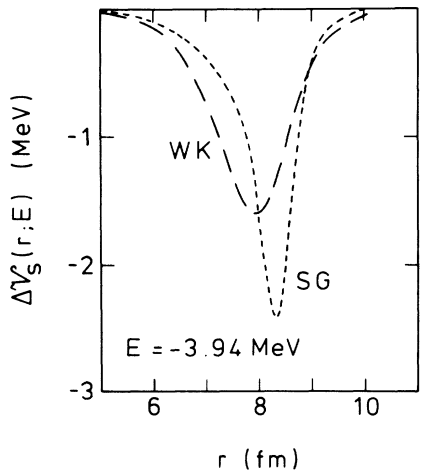

FIG. 9. Surface component of the real part of the mean field at the energy $E_{2g_{9/2}}=-3.94$ MeV. The short dashes correspond to the SG model of Sec. III B, and the long dashes to the WK model of Sec. III C.

present results with those presented in the "hybrid" SG model of Sec. VI of Ref. 2. In this hybrid model, $\mathcal{W}_s(r;E)$ was exactly the same as in the present SG model; however, the real surface component $\Delta\mathcal{V}_s(r;E)$ was not calculated from Eq. (1.10): only the integral form, Eq. (1.11), of the DR was fulfilled. More specifically, the radial shape of $\Delta\mathcal{V}_s(r;E)$ was assumed *a priori* to be given by the derivative of a Woods-Saxon:

$$\Delta\mathcal{V}_d(r;E)=\Delta V_d(E)g(X_d)\ , \tag{3.4}$$

and the shape parameters were set equal to (in fm)

$$r_d=1.35 \text{ for } E<5.8 \text{ MeV}\ , \tag{3.5a}$$

$$r_d=1.35-0.0190(E-5.8) \text{ for } 5.8<E<10 \text{ MeV}\ , \tag{3.5b}$$

$$r_d=1.27 \text{ for } 10 \text{ MeV}<E\ , \tag{3.5c}$$

$$a_d=0.58 \text{ for all } E\ . \tag{3.5d}$$

The strength $\Delta V_d(E)$ was determined in such a way that the volume integral of $\Delta\mathcal{V}_d(r;E)$ is equal to that of $\Delta\mathcal{V}_s(r;E)$, i.e., in such a way that the integral form (1.11) of the DR is fulfilled. The χ^2/N associated with this hybrid SG model are listed in Table II of Ref. 2 and reproduced in column (i) of Table I. They are smaller than in the present SG model for $E<7.0$ MeV. This does not imply that this hybrid model is more meaningful than the present SG model. Indeed, the radial shape (3.4) disagrees with the DR (1.10) (see Sec. V). Furthermore, the values (3.5a)–(3.5d) of the shape parameters adopted in Ref. 2 were determined in such a way as to improve the agreement with the experimental cross sections; it is thus not surprising that the agreement with the experimental data reached in the hybrid SG model of Ref. 2 is better than that obtained in the present, more consistent, SG model, since the hybrid model contains a larger number of adjustable parameters.

Finally, we mention that the hybrid model of Eqs. (3.4)–(3.5d) leads to the same problem as the SG model as far as the single-particle energies are concerned. Indeed, Fig. 18 of Ref. 2 shows that the absolute strength of the predicted real dispersive correction has to be increased in order to reproduce the observed single-particle energies. In both cases, the main origin of this problem lies in the feature that, near the Fermi energy, the real surface component is narrow and peaked beyond the average root-mean-square radius of the valence orbits.

C. Weak energy dependence of r_s and a_s

We argued in the preceding section that in the SG parametrization the parameter r_s takes too large values at low energy, Eq. (3.2a). Therefore, we now consider a model in which the energy dependence of r_s and a_s is weaker than in the SG model. In this WK (for "weak") model, the quantities r_s and a_s are parametrized as follows (in fm):

$$r_s=1.35 \text{ for } E<5 \text{ MeV}\ , \tag{3.6a}$$

$$r_s=1.35-0.0160(E-5) \text{ for } 5<E<10 \text{ MeV}\ , \tag{3.6b}$$

$$r_s = 1.27 \text{ for } 10 \text{ MeV} < E \ , \tag{3.6c}$$

$$a_s = 0.40 \text{ for } E < 5 \text{ MeV} \ , \tag{3.7a}$$

$$a_s = 0.40 + 0.0360(E-5) \text{ for } 5 < E < 10 \text{ MeV} \ , \tag{3.7b}$$

$$a_s = 0.58 \text{ for } 10 \text{ MeV} < E \ . \tag{3.7c}$$

This parametrization is represented by the long-dashed lines in Figs. 3 and 4. The corresponding strength $W_s(E)$ is determined by our requirement that the volume integral of the surface absorption be given by Eqs. (2.5); it is represented by the long-dashed line in Fig. 6.

The differential cross sections predicted by this WK model are given by the dashed curves in Fig. 1. Their agreement with the experimental data is sizably better than that obtained in the SG model (dashed curves in Fig. 7). It is also better than that obtained in the FX model (solid curves in Fig. 1), except at 4 MeV. These features are confirmed by the χ^2/N listed in the column labeled WK in Table I.

In order to study the overall goodness of the WK model, we proceed as in Figs. 2 and 8: we perform two-parameter least-squares fits [see expression (2.4a)] to the experimental cross sections and one-parameter adjustments [see expression (2.4b)] to the observed single-particle energies. The resulting volume integrals are represented by the dots and crosses in Fig. 10. Their overall agreement with the model curves is sizably better than in the case of the FX model (Fig. 1) or of the SG model (Fig. 8). In particular, the model values of the volume integral of $\Delta\mathcal{V}_s(r;E)$ are satisfactory for the unoccupied valence orbits; they are still somewhat too small for the occupied orbits. A plausible explanation is the following. The average root-mean-square radius is larger for the unoccupied valence orbits (7.32 fm, see Table V of Ref. 2) than for the occupied orbits (6.17 fm). Figure 9 shows that near the Fermi energy, the model

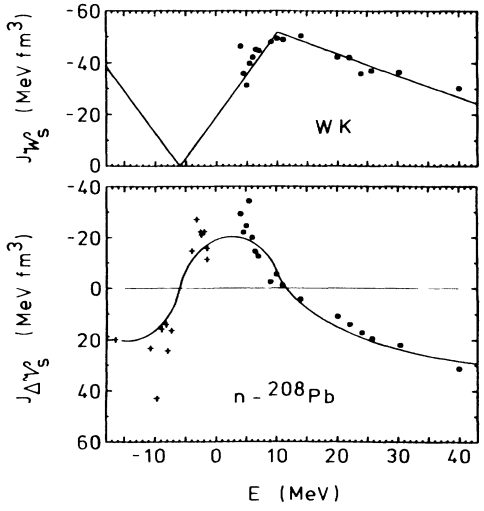

FIG. 10. Same as Fig. 8, except that the dots and crosses are now obtained from the WK model of Sec. III C. The model curves are the same as in Figs. 2 and 8.

$\Delta\mathcal{V}_s(r;E)$ peaks at $R_s = 7.90$ fm, and approximately has the radial shape $g(X_f)$ with $R_f = 7.90$ fm, $a_f = 0.52$ fm. Hence the overlap of $\Delta\mathcal{V}_s(r;E)$ with the single-particle orbits is larger in the case of the unoccupied than of the occupied valence orbits. This suggests that the assumed value of r_s at small energy is still too large in the WK model.

IV. ANGULAR-MOMENTUM-DEPENDENT SURFACE ABSORPTION

A. Introduction

In Sec. VII of Ref. 2, the surface absorption was allowed to depend upon the angular momentum L of the incoming neutron. The radius r_s of the surface absorption is held fixed as in the FX model, viz.,

$$r_s = 1.27 \text{ fm} \ . \tag{4.1}$$

The partial waves were divided into two groups: "group (b)" contains the partial waves with $L = 1$, 3, and 6, while "group (c)" contains all the other partial waves. The origin of this grouping was that empirical fits indicated that, below 11 MeV, the volume integral of $\mathcal{W}_s(r;E)$ for group (b) is systematically larger, in absolute magnitude, than that of group (c). The following parametrization was used in the case of group (b) (in units MeV fm^3):

$$J_{\mathcal{W}_s} = 0 \text{ for } -6 < E < -2 \text{ MeV} \ , \tag{4.2a}$$

$$J_{\mathcal{W}_s} = -6.44(E+2) \text{ for } -2 < E < 6.5 \text{ MeV} \ , \tag{4.2b}$$

$$J_{\mathcal{W}_s} = -0.835(72-E) \text{ for } 6.5 < E < 72 \text{ MeV} \ , \tag{4.2c}$$

$$J_{\mathcal{W}_s} = 0 \text{ for } 72 \text{ MeV} < E \ . \tag{4.2d}$$

In the case of group (c), the parametrization was the following:

$$J_{\mathcal{W}_s} = 0 \text{ for } -6 < E < -5 \text{ MeV} \ , \tag{4.3a}$$

$$J_{\mathcal{W}_s} = -2.95(E+5) \text{ for } -5 < E < 12 \text{ MeV} \ , \tag{4.3b}$$

$$J_{\mathcal{W}_s} = -0.835(72-E) \text{ for } 12 < E < 72 \text{ MeV} \ , \tag{4.3c}$$

$$J_{\mathcal{W}_s} = 0 \text{ for } 72 \text{ MeV} < E \ . \tag{4.3d}$$

These parametrizations will be adopted in the present section. They are represented by the solid and dashed linear segments in the upper part of Fig. 11. The strengths $W_s(E)$ of the surface absorption for these two groups are specified by the requirement that the volume integrals of $\mathcal{W}_s(r;E)$ are given by Eqs. (4.2a)–(4.3d).

B. Strong energy dependence of a_s

We first investigate a model in which the diffuseness has the same strong energy dependence as in the SG model, Eqs. (3.3). We recall that the radius parameter r_s is independent of energy, as specified by Eq. (4.1). We denote this model by "L-SGa_s" to signify that the surface absorption depends upon the orbital angular momentum

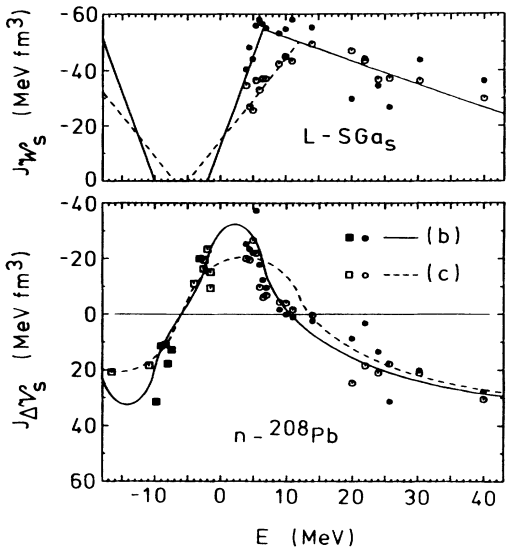

FIG. 11. Energy dependence of the volume integrals per nucleon of the imaginary (top) and real (bottom) components of the mean fields in the case of the L-SGa_s model of Sec. IV B. The symbols are obtained by multiplying the surface components of the model by renormalization factors, expression (2.4a), and by adjusting the latter to a best least-squares fit to the experimental cross section at that energy; the solid dots correspond to group (b) and the open symbols to group (c). At negative energies the symbols give the volume integral of surface component renormalized in such a way as to reproduce the observed energies of the single-particle states, expression (2.4b); the solid symbols correspond to the levels of group (b) and the open symbols to those of group (c). The lines are the same as in Fig. 22 of Ref. 2.

L, while the diffuseness a_s strongly depends upon energy. As in the previous models the real surface contribution $\Delta\mathcal{V}_s(r;E)$ is determined from the DR, Eq. (1.10), by numerical integration performed for the two angular momentum groups, separately.

The differential cross sections predicted by this L-SGa_s model are represented by the solid curves in Fig. 7, and the associated χ^2/N are listed in the column labeled L-SGa_s in Table I. We see that the agreement with the experimental data is comparable to that reached in the FX model (solid curves in Fig. 2) and in the SG model (dashed curves in Fig. 7); correspondingly, the χ^2/N are comparable for the three models.

To gain further insight we proceed in a similar way as in Figs. 2, 8, and 10: we renormalized the surface potentials in order to reproduce the binding energies of the single-particle states and to best fit the differential, total, and polarization data by least squares. In the present case, however, there are two expressions like (2.4a) because there exist two groups of partial waves. Thus, for positive energies there are four parameters to be adjusted by least squares. For negative energies the $\Delta\mathcal{V}_s(E)$ for the group having the L value of the bound state is inserted into expression (2.4b), and the renormalization factor is adjusted to reproduce the binding energy. The resulting volume integrals are represented by the symbols in Fig. 11, with round symbols for $E>0$ and squares for $E<0$.

The upper part of Fig. 11 confirms that, for $E<12$ MeV, the volume integral of the surface absorption is larger for group (b) than for group (c). The solid and open symbols are in fair agreement with the solid and dashed lines, i.e., with Eqs. (4.2a)–(4.2c) and (4.3a)–(4.3c), respectively. This agreement is not trivial since these linear segments are reproduced from Ref. 2, where they were derived from different least-squares fits, as will be recalled below.

The lower part of Fig. 11 shows that the symbols associated with the bound single-particle states lie closer to the predictions of the DR than was the case for the SG model; compare with Fig. 8. This improvement is a consequence of the constant value now adopted for the radius parameter, Eq. (4.1). For low positive energies ($E<11$ MeV), the solid points for group (b) follow the predicted solid curve rather closely, while the open symbols for group (c) fall slightly below the predicted dashed curve. The fact that the symbols for $E>11$ MeV are more scattered than in Figs. 2, 8, and 10, in both the upper and lower parts, is associated with the existence of four rather than only two adjustable parameters.

One can obtain clues for improvement of the model by comparing with the L-dependent "hybrid" L-SGa_s model which had been considered in Sec. VII of Ref. 2. There, the surface absorption was exactly the same as in the present model; however, the detailed DR, Eq. (1.10), was not fulfilled. Indeed, it was requested that only its integral form, Eq. (1.11), be satisfied. More specifically, the radial shape of $\Delta\mathcal{V}_s(r;E)$ in this hybrid L-Sga_s model was *a priori* assumed to have the radial shape of Eq. (3.6), with the following shape parameters (in fm):

$$r_d=1.27 \quad \text{for all } E\ , \tag{4.4a}$$

$$a_d=0.20+0.0238(E+6) \quad \text{for } -6<E<10 \text{ MeV}\ , \tag{4.4b}$$

$$a_d=0.58 \quad \text{for } 10 \text{ MeV}<E\ . \tag{4.4c}$$

The strengths $\Delta V_d(E)$ for groups (b) and (c) were determined by the requirement that the volume integrals of $\mathcal{W}_s(r;E)$ and $\Delta\mathcal{V}_s(r;E)$ must fulfill the DR (1.11). The values of χ^2/N obtained from this hybrid L-SGa_s model are listed in Table II of Ref. 2 and reproduced in the column labeled (ii) in Table I. They are smaller than in the present L-SGa_s model. However, this is not very meaningful since the radial shape of $\Delta\mathcal{V}_s(r;E)$ assumed in Ref. 2 is not consistent with the DR (1.10). Furthermore, the parameters (4.4) of the assumed radial shape of $\Delta\mathcal{V}_s(r;E)$ were chosen in such a way as to optimize the quality of the fits to the experimental scattering data. In other words, the hybrid L-SGa_s model of Ref. 2 contained more adjustable parameters than the present, more consistent, L-SGa_s model.

The fact that the present L-SGa_s model gives a much worse fit to angular distributions than the hybrid L-SGa_s model of Ref. 2 is attributed primarily to the fact that in

the present model the dispersive component $\Delta\mathcal{V}_s(r;E)$ strongly depends upon r. For energies close to 6.5 MeV, for example, $\Delta\mathcal{V}_s(r;E)$ has a surface attractive (negative) minimum between two positive maxima, as we shall demonstrate in Sec. V. This contrasts with the hybrid model in which $\Delta\mathcal{V}_s(r;E)$ has a simple radial shape, see Eqs. (4.4). Since the strong radial dependence of $\Delta\mathcal{V}_s(r;E)$ is a consequence of the strong energy dependence assumed for a_s, one can reasonably conclude that the agreement with the experimental data can be improved by assuming a weaker energy dependence of a_s. This is discussed in the following section.

C. Weak energy dependence of a_s

We now consider a model which differs from the L-SGa_s model of the preceding subsection only in that a_s will now have the weak energy dependence defined by Eqs. (3.7). We call this the "L-WKa_s" model, meaning "L-dependent surface absorption with weakly energy-dependent diffuseness a_s."

The differential cross sections predicted by this L-WKa_s model are represented by dashed curves in Fig. 12 and the associated χ^2/N are listed in the column labeled L-WKa_s in Table I. The agreement with the experimental data is seen to be better than in the L-SGa_s model at all scattering energies and comparable to the hybrid L-SGa_S model at most energies. This in keeping with the discussion in the preceding section.

Figure 13 shows the results of renormalization searches analogous to those in Fig. 11. These results are quite similar to those shown in Fig. 11, with the main difference that, for $E < 10$ MeV, the solid symbols for $J_{\mathcal{W}_s}$ now lie closer to the parametrization of Eqs. (4.2) and (4.3).

D. Fixed geometry

The comparison between the results obtained in Secs. IV B and IV C respectively, indicates that the experimental data do not favor the use of a strongly energy-dependent radial shape of the surface absorption when one takes due account of the DR between the real and imaginary surface components. We now investigate to what extent the division of the partial waves into two groups enables one to avoid the use of an energy-dependent radial shape of the surface absorption. We thus set the shape parameters to the same constant values as in Eq. (2.1). We retain the same two groups (b) and (c) of partial waves as in Ref. 2, and also the same volume integrals of the surface absorption as in Eqs. (4.2a)–(4.3d). We refer to this model as the "L-FX" model, for "L-dependent surface absorption with fixed radial shape."

The differential cross sections predicted by this L-FX model are given by the solid curves in Fig. 12, and the values of χ^2/N are contained in the last column of Table I. The agreement with the experimental data is almost as good as in the L-WKa_s model, except at the three lowest energies for which it is rather poor. The latter feature is reflected in Fig. 14, in which the corresponding volume

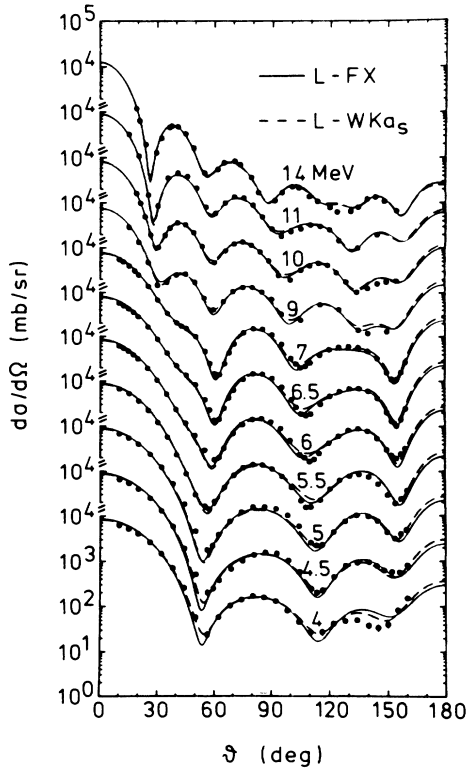

FIG. 12. Angular dependence of the differential n-^{208}Pb cross sections. The dots are the same experimental values as in Fig. 2. The dashed curves represent the predictions of the L-WKa_s model of Sec. IV C and the solid curves those of the L-FX model of Sec. IV D.

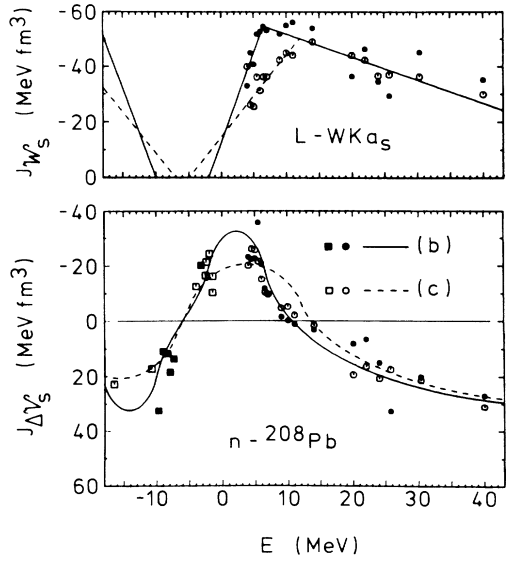

FIG. 13. Same as Fig. 11, except that the solid and open symbols are now obtained from the L-WKa_s model (Sec. IV C) instead of the L-SGa_s model. The lines are the same as in Fig. 11.

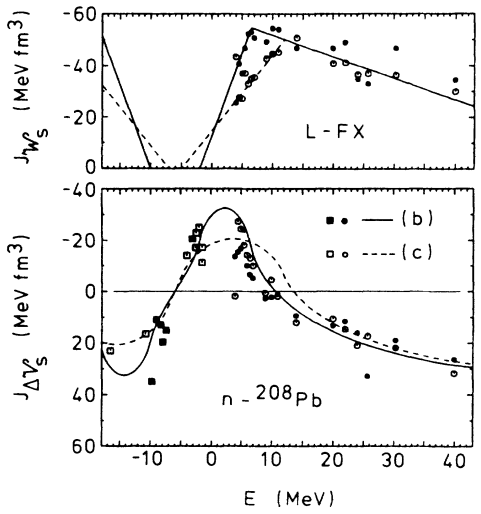

FIG. 14. Same as Fig. 11, except that the solid and open symbols are now obtained from the L-FX model (Sec. IV D) instead of the L-SGa_s model.

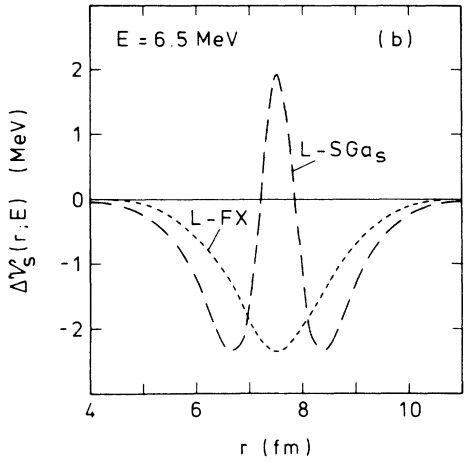

FIG. 15. Radial dependence of the real surface component $\Delta\mathcal{V}_s(r;E=6.5\ \text{MeV})$, for the partial waves of group (b). The short-dashed curve corresponds to the L-FX model of Sec. IV D. The long-dashed line is computed from the L-SGa_s model of Sec. IV B.

integrals of the imaginary or real surface components lie rather far away from the solid curves.

On the average, however, the L-FX model leads to satisfactory agreement with the experimental data. This is quite remarkable in view of the small number of parameters which appear in this model.

V. RADIAL SHAPE OF THE REAL SURFACE COMPONENT

In the preceding sections as in most empirical analyses, the radial shape of the surface absorption $\mathcal{W}_s(r;E)$ was assumed to be the derivative of a Woods-Saxon form factor, Eq. (1.9b). However, this does not imply that the real surface component $\Delta\mathcal{V}_s(r;E)$ also has a similar shape. Indeed, the DR (1.10) expresses the real surface contribution $\Delta\mathcal{V}_s(r;E)$ in terms of the surface potential $\mathcal{W}_s(r;E')$ at *all* energies E'. Hence, the radial shape of $\Delta\mathcal{V}_s(r;E)$ at the energy E can be quite different from that of $\mathcal{W}_s(r;E)$ at the same energy E. This is illustrated in the present section.

We first consider parametrizations of $\mathcal{W}_s(r;E)$ in which the radius parameter $r_s=1.27$ fm is independent of energy, as in the models studied in Sec. IV. Then, the DR (1.10) implies that $\Delta\mathcal{V}_s(r;E)$ is symmetric about $R_s=7.52$ fm. The short-dashed curve in Fig. 15 has been calculated from the L-FX model of Sec. IV D, in which the shape of $\mathcal{W}_s(r;E)$ is independent of energy. Then, $\Delta\mathcal{V}_s(r;E)$ has the same shape $g(X_s)$ as $\mathcal{W}_s(r;E)$; see Eqs. (1.9) and (2.2). This changes drastically when the diffuseness parameter of $\mathcal{W}_s(r;E)$ depends upon energy. This is exhibited by the long-dashed curve in Fig. 15, which is associated with the L-SGa_s parametrization of Eqs. (3.7) for $a_s(E)$. We emphasize that the two curves in Fig. 15 correspond to exactly the same volume integral.

This peculiar radial shape of $\Delta\mathcal{V}_s(r;E)$ at small E in the L-SGa_s model can be understood as follows. For $E'<E$ the integrand in the DR (1.10) is positive and narrow [since $a_s(E')$ is small]; an example is shown by the short-dashed curve in Fig. 16. For $E'>E$, the integrand in the DR (1.10) is negative and broad; an example is given by the long-dashed curve in Fig. 16. Hence the value of $\Delta\mathcal{V}_s(r;E)$ in the energy domain $0\lesssim E\lesssim 14$ MeV derives from the sum of narrow positive peaks and of broad negative pockets. This gives rise to a narrow hump superimposed on a broad attractive dip, as illustrated by the long-dashed curve in Fig. 15.

This peculiar shape of $\Delta\mathcal{V}_s(r;E)$ persists when one adopts a weaker energy dependence of the diffuseness a_s. This is displayed in Fig. 17, which is associated with the L-WKa_s model of Sec. IV C. In this case, however, the

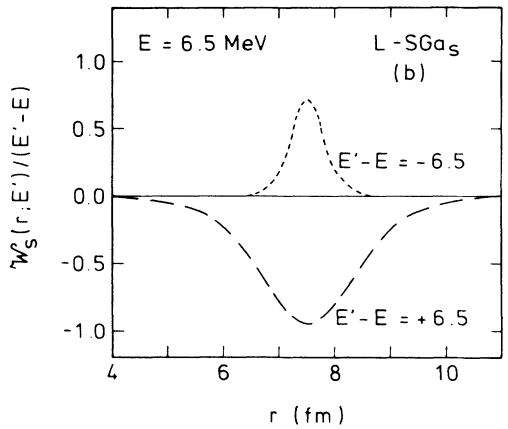

FIG. 16. Radial dependence of the integrand in the DR (1.10) in the case of group (b) of the L-SGa_s model of Sec. IV B, for $E=6.5$ MeV. The short-dashed curve corresponds to $E'-E=-6.5$ MeV and the long-dashed curve to $E'-E=+6.5$ MeV.

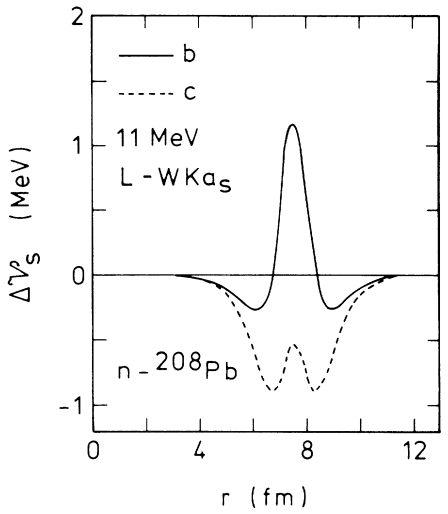

FIG. 17. Radial dependence of the real surface component $\Delta\mathcal{V}_s(r;E=11$ MeV) for the L-WKa_s model of Sec. IV C. The solid curve is associated with group (b) and the short-dashed line with group (c).

hump near R_s is less narrow than in the L-SGa_s model (note the difference in the abscissa scales of Figs. 15 and 17). Figure 17 also exhibits the fact that at low energy the surface dispersive component is quite different for groups (b) and (c), respectively.

When, in addition to a_s, the radial parameter r_s of $\mathcal{W}_s(r;E)$ depends upon energy, the radial shape of $\Delta\mathcal{V}_s(r;E)$ becomes even more complicated. This is illustrated in Figs. 18 and 19. Let us first consider Fig. 18, which is associated with the SG model of Sec. III B. For small values of E, the integrand of the DR (1.10) involves

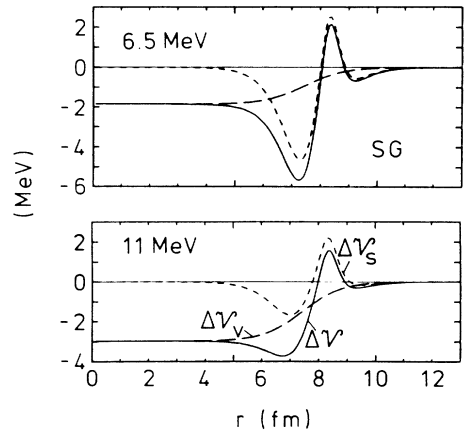

FIG. 18. Radial dependence of the dispersive contributions to the real part of the mean field in the case of the SG model of Sec. III B, for the energies $E=6.5$ MeV (top) and $E=11$ MeV (bottom). The short-dashed curves represent the surface components, the long-dashed lines the volume (Woods-Saxon shaped) components (same as in Ref. 2), and the solid curves the sum of these two contributions.

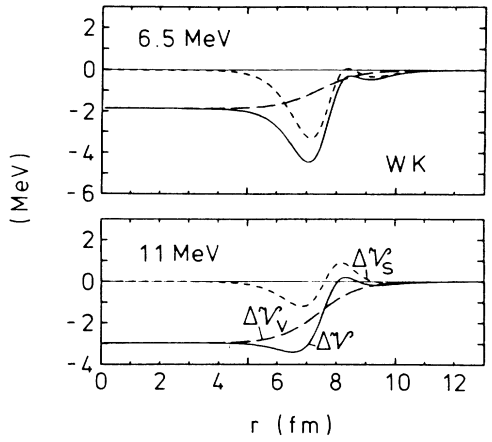

FIG. 19. Same as Fig. 18, for the WK model of Sec. III C.

positive contributions which are narrow and peaked at large distance [≈ 8.3 fm, see Eq. (3.2a)], and negative contributions which are broad and centered at a smaller distance [≈ 7.5 fm, see Eqs. (3.2c)]. The combined effect of these two contributions leads to the wiggle represented by the short-dashed curves in Fig. 18.

These complicated shapes of $\Delta\mathcal{V}_s(r;E)$ occur only for small positive values of E. For E negative and close to the Fermi energy, the radial shape of $\Delta\mathcal{V}_s(r;E)$ is mainly determined by the shape of $\mathcal{W}_s(r;E')$ for $|E'-E|<20$ MeV. It is thus a sum of attractive peaks. These are narrow and centered near 8.3 fm in the SG model; they are broader and centered near 8 fm in the WK model. This explains the shape of the two curves that had previously been shown in Fig. 9.

The effect of the dispersive contribution on the radial shape of the real part of the full mean field is illustrated in Fig. 20. In the case of a weakly energy-dependent radial shape of $\mathcal{W}_s(r;E)$, the surface component $\Delta\mathcal{V}_s(r;E)$

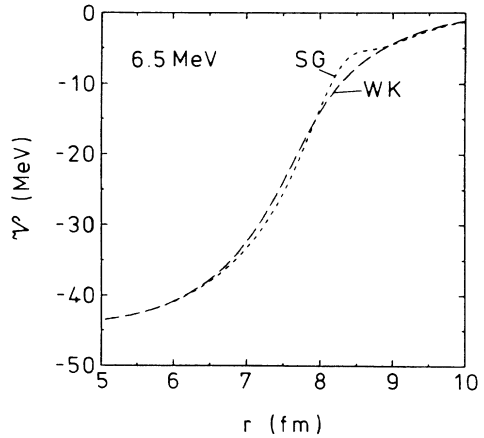

FIG. 20. Radial dependence of the real part of the full mean field at 6.5 MeV. The short-dashed curve corresponds to the SG model of Sec. III B and the long-dashed curve to the WK model of Sec. III C.

is fairly broad and is centered not far from the radius $R_H = 7.35$ fm of the volume contribution $\mathcal{V}_H(r;E) + \Delta\mathcal{V}_v(r;E)$ [see Eqs. (1.4a) and (1.7′) and Ref. 2]. Then, the full potential approximately has a Wood-Saxon shape, as illustrated by the long-dashed curve in Fig. 20. In contrast, $\Delta\mathcal{V}_s(r;E)$ has a marked wiggle in the SG model (Fig. 18). Then, the radial shape of the full potential sizably deviates from a Woods-Saxon; this is illustrated by the short-dashed curve in Fig. 20.

VI. SUMMARY AND DISCUSSION

For low bombarding energies the imaginary part of the phenomenological local optical-model potential is peaked at the nuclear surface. This surface absorption $\mathcal{W}_s(r;E)$ is usually assumed to be proportional to the derivative of a Woods-Saxon form factor, see Eqs. (1.9). Phenomenological optical-model analyses of recent accurate experimental cross sections for neutron scattering from ^{89}Y (Ref. 4), ^{208}Pb (Refs. 8 and 9), ^{209}Bi (Ref. 6), ^{59}Co (Ref. 5), and ^{51}V (Ref. 7) show that the radial shape of $\mathcal{W}_s(r;E)$ depends upon energy for E smaller than about 10 MeV. This is confirmed by the compilation of n-^{208}Pb optical-model potentials presented in Figs. 3 and 4. In particular the diffuseness a_s associated with the width of $\mathcal{W}_s(r;E)$ sharply decreases with decreasing energy in the domain $4 \lesssim E \lesssim 10$ MeV.

The DR (1.10) implies that the real part of the mean field contains a surface component, $\Delta\mathcal{V}_s(r;E)$, which can be calculated from the imaginary part $\mathcal{W}_s(r;E)$. When the radial shape of $\mathcal{W}_s(r;E')$ depends upon E', that of $\Delta\mathcal{V}_s(r;E)$ also depends upon energy. Initially the main purpose of the present study was to calculate $\Delta\mathcal{V}_s(r;E)$ for several parametrizations of the energy dependence of the radial shape of $\mathcal{W}_s(r;E')$. This has to be done numerically and had not been performed until now.

Examples of calculated values of $\Delta\mathcal{V}_s(r;E)$ are shown in Figs. 15 and 17 (in cases when the diffuseness a_s depends upon energy and the location R_s of the surface absorption in constant) and in Figs. 9, 18, and 19 (in cases when both the location R_s and the diffuseness a_s of the surface absorption depend upon energy). The radial shape of $\Delta\mathcal{V}_s(r;E)$ at small positive E is seen to be rather complicated. The origin of this finding is explained in Sec. V (see Fig. 16). This calculated shape is quite different from the one that had been assumed in Secs. VI and VII of Ref. 2. We have thus been led to compute and compare with experiment the differential cross sections associated with our calculated $\Delta\mathcal{V}_s(r;E)$ since these "hybrid" models used in Ref. 2 were not fully consistent. We have also computed total and polarization cross sections but did not show these in our paper because they do not modify the conclusions that can be drawn from the differential cross sections alone.

Our primary purpose in Secs. III and IV was thus to investigate the influence of the radial shape of $\Delta\mathcal{V}_s(r;E)$ on the n-^{208}Pb differential cross sections. In order to focus on this effect we always retained exactly the same volume- (Woods-Saxon) shaped components of the complex mean field as in Ref. 2; we also always retained exactly the same volume integrals of the real and imaginary surface component $\Delta\mathcal{V}_s(r;E)$ and $\mathcal{W}_s(r;E)$.

In the SG model of Sec. III B the surface absorption $\mathcal{W}_s(r;E)$ is the same as in Sec. VI of Ref. 2. The only difference is that here the radial shape of $\Delta\mathcal{V}_s(r;E)$ is calculated from the DR (1.10), while in Ref. 2 it was *a priori* assumed to be the derivative of a Woods-Saxon. In both cases the volume integral of $\Delta\mathcal{V}_s(r;E)$ is exactly the same. Thus, the radial shape of $\Delta\mathcal{V}_s(r;E)$ is the sole source of the difference between the χ^2/N listed in the columns respectively labeled SG and (i) in Table I. The calculated differential cross sections are seen to be quite sensitive to the radial shape of $\Delta\mathcal{V}_s(r;E)$, although this surface component is quite weak (its volume integral per nucleon is smaller than 20 MeV fm^3). This opens the possibility of investigating in detail small components of the mean field.

In the SG model the energy dependence of the diffuseness is quite strong. It gives rise to a pronounced wiggle in the radial dependence of $\Delta\mathcal{V}_s(r;E)$ at low energy (Fig. 18), and relatedly to a marked deviation of the full real part from a Woods-Saxon shape (Fig. 20). The agreement between predicted and experimental cross sections is then rather poor (Fig. 7). Between 4 and 5.5 MeV it is even less good than in the FX model of Ref. 2 (Sec. II) in which the radial shape of $\mathcal{W}_s(r;E)$ is independent of energy. In the SG model the real surface component $\Delta\mathcal{V}_s(r;E)$ is quite narrow in the vicinity of the Fermi energy, where it is furthermore located outside the nuclear surface (Fig. 9). As a consequence the real surface component $\Delta\mathcal{V}_s(r;E)$ has too small an overlap with the orbits of the bound single-particle states. This is reflected by the systematic deviation of the crosses from the solid curve in the lower part of Fig. 8.

In view of these defects of the SG model, we constructed in Sec. III C a model in which the energy dependence of the radial shape of the surface absorption is weak. This WK model yields good fits to the experimental cross sections (Fig. 2): the corresponding values of χ^2/N are smaller than those of the SG model by approximately a factor of 2. For negative energies, however, the overlap of the predicted $\Delta\mathcal{V}_s(r;E)$ with the single-particle orbits is still somewhat too small (see the crosses in Fig. 10).

From the above discussion we conclude that the dispersive optical-model analysis of the scattering cross sections indicates that for $E < 10$ MeV the diffuseness a_s of the surface absorption decreases with decreasing energy, but that this decrease is weaker than the one assumed in the SG parametrization of Sec. VI of Ref. 2. On the other hand, the comparison between the predicted and experimental single-particle energies suggests that it is not justified to assume that the radius R_s of the surface absorption increases with decreasing energy. Therefore we investigated models in which the radius R_s of the surface absorption is independent of energy. We checked that if one sets R_s constant (while letting a_s depend upon energy) in models of the type studied in Sec. III the fits to the differential cross sections are worsened. This is why we turned in Sec. IV to models in which R_s is a constant but in which the surface absorption depends upon the or-

bital angular momentum of the incident nucleon. This possibility had been suggested in Ref. 10 and studied in more detail in Refs. 2 and 11.

In order to facilitate comparison we adopted in Sec. IV the same type of angular momentum dependence as in Sec. VII of Ref. 2, namely we assumed that $\mathcal{W}_s(r;E)$ takes one value for the neutron orbital angular momenta $L=1,3,6$ [group (b)], and another one for all the other orbital angular momenta [group (c)]. Furthermore we retained the same parametrization as in Sec. VII of Ref. 2 for the volume integral of $\mathcal{W}_s(r;E)$ for groups (b) and (c), respectively.

In Sec. IV B we used exactly the same surface absorption $\mathcal{W}_s(r;E)$ as in Sec. VII of Ref. 2, namely one in which the radius is independent of energy ($R_s=1.27$ fm), while between 2.6 and 10 MeV the diffuseness a_s has the same strong dependence upon energy as in Sec. III B. This L-SGa_s model does not yield good fits to the experimental cross sections (Fig. 7). The corresponding χ^2/N are much larger than those which had been obtained in Sec. VII of Ref. 2 [see column (ii) of Table I]. There, the radial shape of $\Delta\mathcal{V}_s(r;E)$ was assumed *a priori* to be the derivative of a Woods-Saxon, with a diffuseness $a_d(E)$ adjusted to yield optimal fits to the experimental data; we have shown that these assumptions are not compatible with the DR (1.10) (see Fig. 15).

This failure of the L-SGa_s model can be ascribed to the fact that the strong energy dependence of $a_s(E)$ yields a sharp wiggle in the radial dependence of $\Delta\mathcal{V}_s(r;E)$; this leads to a full potential whose shape is sizably different from a Woods-Saxon (Fig. 20). This led us to consider in Sec. IV C a model in which $a_s(E)$ has the same weak energy dependence as in Sec. III C; as in Sec. IV B the radius parameter is kept constant ($r_s=1.27$ fm) and the partial waves are divided into the two groups (b) and (c). This L-WKa_s model yields good fits to the differential cross sections (Fig. 12). This indicates that one can keep r_s constant at low energy provided that one allows the surface absorption to depend upon the angular momentum of the incident nucleon. The origin of this property is discussed in Ref. 11.

The agreement between the predicted and experimental single-particle energies (see Figs. 11 and 13) is better in Secs. IV B and IV C than in the models of Secs. III B and III C. Hence the models in which the radius R_s is constant but $\mathcal{W}_s(r;E)$ depends upon angular momentum are globally better than those in which R_s depend upon energy and $\mathcal{W}_s(r;E)$ is independent of angular momentum. This led us to investigate in Sec. IV D a relatively simple model, the L-FX model, in which the radial shape of the surface absorption is fixed but depends upon the orbital angular momentum L. This L-FX model yields fair agreement with the experimental cross sections (Fig. 12) and satisfactorily predicts the single-particle energies (Fig. 14). We note that this model has the same operational virtue as the original FX model in that the DR can be evaluated analytically. Also, it is simple in that it involves fewer empirical functions of energy than all but the original FX model.

We conclude that in the case n-^{208}Pb there exists good evidence that at low energy (i) the surface absorption $\mathcal{W}_s(r;E)$ depends upon the angular momentum of the incoming neutron, and (ii) the diffuseness a_s of $\mathcal{W}_s(r;E)$ slightly decreases with decreasing energy below about 10 MeV. These conclusions are based on a detailed comparison between the experimental data and the predictions of the dispersive optical-model potential. Note that it was important to extend this comparison to negative energies. Indeed, this extension provides the main basis for believing that it is more plausible to assume that $\mathcal{W}_s(r;E)$ depends upon angular momentum than to assume that the radius R_s of $\mathcal{W}_s(r;E)$ depends upon energy.

We finally turn to a brief discussion of possible microscopic interpretation of our findings. This discussion can only be qualitative since there exists no reliable theoretical evaluation of the imaginary part of the mean field at low energy. It is known empirically that at low energy the imaginary part of the optical-model potential is peaked at the nuclear surface. This demonstrates that at low energy the single-particle degree of freedom is predominantly coupled to the low-lying collective excitations of the nuclear surface. This coupling is schematically represented by the diagrams of Fig. 21. In (a) the incoming neutron n excites a collective vibration λ' of the ^{208}Pb core and falls in an orbit labeled n'; note that this orbit can belong to the continuum. Graph (a) of Fig. 21 thus accounts for the imaginary part that arises from direct inelastic scattering. This contribution has been evaluated in Ref. 12 in the framework of a self-consistent random-phase approximation based on Skyrme-type effective interactions. The most important collective excitations λ' at low energy are the low-lying 3^-, 5^-, 2^+, and 4^+ isoscalar levels in ^{208}Pb. These have a transition density that is approximately proportional to $d\rho/dr$,

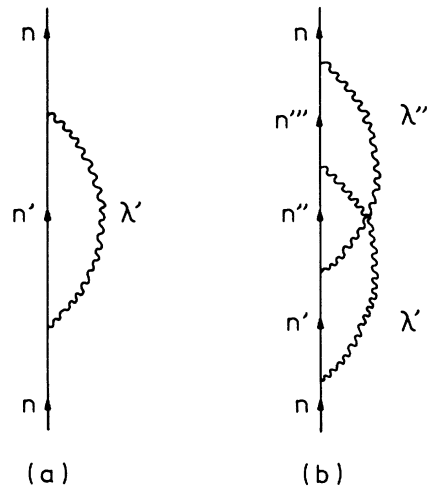

FIG. 21. Contributions of collective core excitations to the mean field. In (a) an incident neutron with quantum numbers generically denoted by n excites a collective mode λ' of the core and falls in an orbit with quantum numbers n'. In (b) this initial step is followed by the excitation of another collective mode λ''.

where $\rho(r)$ is the density distribution in the ^{208}Pb ground state. The contributions of these excited states to $\mathcal{W}_s(r;E)$ are roughly proportional to $(d\rho/dr)^2$ [see Eq. (9) of Ref. 12]; the density dependence of the effective interaction pushes the absorption peak towards larger radial distances but this peak remains quite narrow: the calculated $\mathcal{W}_s(r;E)$ is peaked near 7.3 fm ($r_s \approx 1.23$ fm), with a diffuseness $a_s \approx 0.25$ fm.[12] This diffuseness slightly increases with increasing neutron energy;[13] this trend is in keeping with one of our semiphenomenological findings. It reflects the decreasing relative importance of the first 3^- excitation of ^{208}Pb as the bombarding energy increases.

The theoretical calculation of Ref. 12 underestimates the absorption. At low energy, the processes that should be blamed for this underestimate most probably correspond to multiple excitations, of the type described by diagram (b) of Fig. 21. This type of absorption gives rise to complicated intermediate states, i.e., essentially to compound nucleus formation. It is important to notice that in the contribution shown in Fig. 21 the interactions all occur at the nuclear surface.

From this discussion, we conclude that at low energy the absorption mainly arises from surface excitations of the ^{208}Pb core, and that at very low energies the excited 3^- state at 2.6 MeV dominates, i.e., provides the main doorway to the feeding of the compound nucleus. Note that this would explain the trend that, at low energy, the diffuseness a_s of the surface absorption increases with energy as assumed in the WK model, since any combined influence of several collective excitations would necessarily broaden the surface absorption peak.

We now turn to the possible origin of the property that the surface absorption depends upon the angular momentum of the incident neutron, as in the models of Sec. IV. Below 10 MeV the main contributing partial waves correspond to the orbital angular momenta $L = 1-6$. Indeed, Fig. 19 of Ref. 2 shows that the partial waves with $L = 0$ and with $L > 6$ only play a minor role.

The radial parts of the wave functions of these operative partial waves are represented in Fig. 22, for $E = 6.5$ MeV. This energy has been shown because it is the one for which the difference between the surface absorptions for groups (b) and (c) is maximum (see, e.g., Fig. 13). Figure 22 shows that the wave functions of the dominant partial waves of group (c), namely the $d_{5/2}$, $d_{3/2}$, $g_{9/2}$, and $g_{7/2}$ wave functions, all present a node between 7.7 and 8.6 fm, i.e., within the radial domain where the core surface vibrations can be excited. Note that this radial domain lies beyond the nuclear surface because of the density dependence of the effective particle-hole interaction.[12] Accordingly, these core vibrations cannot be efficiently excited by the partial waves of group (c) for incident neutrons with low energy, and the surface absorption is expected to be weak for these partial waves. This is to be contrasted with the main partial waves of group (b). Indeed, the $p_{3/2}$, $p_{1/2}$, $f_{7/2}$, and $f_{5/2}$ wave functions tend to have antinodes in the radial domain where the main wave functions of group (c) have nodes.[11] Hence it appears plausible that they can more efficiently excite the core surface vibrations. This would provide a qualitative explanation for the property that, at low energy, the strength of the surface absorption is on the average weaker for the partial waves of group (c) than for those of group (b).

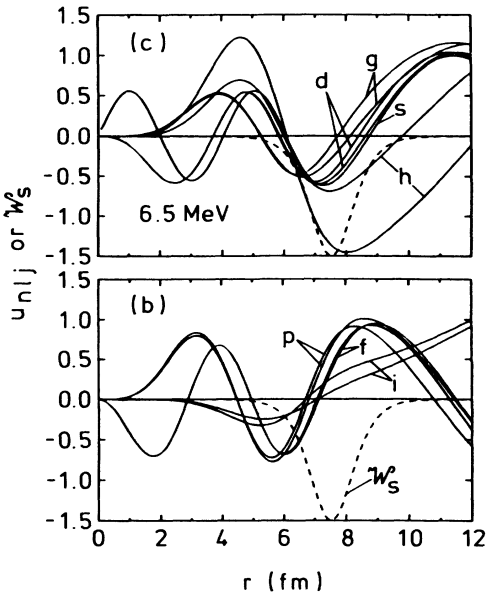

FIG. 22. Radial parts of the scattering wave functions at 6.5 MeV as calculated from the volume-shaped (Woods-Saxon) real mean field $\mathcal{V}_H(r;E)+\Delta\mathcal{V}_v(r;E)$ of Ref. 2 [see Eqs. (1.4a) and (1.7′)]. These wave functions are normalized to unit amplitude at large distance. The lower drawing contains the wave functions of group (b). The upper drawing gathers the main wave functions of group (c) [we observed that the location of the modes of the h wave functions near 11 fm move inwards by as much as 1 fm when $\Delta\mathcal{V}_s(r;E)$ is included in the real mean field, in contrast to the other modes which remain stable]. The dashed curve represents the radial shape of the surface absorption at 6.5 MeV in the L-WKa_s model of Sec. IV C ($R_s = 7.52$ fm, $a_s = 0.454$ fm).

Finally, we note that a dependence of $\mathcal{W}_s(r;E)$ upon angular momentum amounts to introducing a nonlocality in the surface absorption. This type of nonlocality is associated with channel coupling rather than with exchange effects.[14] Schematically, it amounts to expanding the nonlocal potential in the form [see Eq. (8) of Ref. 12]

$$\mathcal{W}_s(\mathbf{r},\mathbf{r}';E)=\sum_{LM}\mathcal{W}_s^L(r,r';E)Y_{LM}(\hat{r})Y_{LM}^*(\hat{r}')\ , \quad (6.1a)$$

and to assuming that

$$\mathcal{W}_s^L(r,r';E)=\mathcal{W}_s^L(r;E)\delta(r-r')\ . \quad (6.1b)$$

Here we omitted complications associated with spin. The angular-momentum-dependent quantity $\mathcal{W}_s^L(r;E)$ fulfills a dispersion relation, as is apparent from Eq. (9) of Ref. 12. The nonlocality associated with channel coupling therefore does not affect the validity of the DR.

In conclusion, we have shown that the dispersive optical-model analysis yields detailed information on the surface components of the n-^{208}Pb mean field at low energy. This has been possible because the differential cross sections are sensitive to the radial shape of the surface component of the real part of the mean field although this component is quite weak. Our analysis provides support for a model in which, below 10 MeV, the real and imaginary surface components depend upon the angular momentum of the incident neutron. Furthermore, the diffuseness of the surface absorption appears to slightly decrease with decreasing energy below 10 MeV.

ACKNOWLEDGMENTS

We are very grateful to Dr. G. R. Satchler and Dr. R. R. Winters for useful discussions. Oak Ridge National Laboratory is operated by Martin Marietta Energy Systems, Inc. for the U.S. Department of Energy under Contract No. DE-AC05-84OR21400.

[1]C. Mahaux and R. Sartor, Nucl. Phys. **A468**, 193 (1987).
[2]C. H. Johnson, D. J. Horen, and C. Mahaux, Phys. Rev. C **36**, 2252 (1987).
[3]C. H. Johnson and C. Mahaux, Phys. Rev. C **38**, 2589 (1988).
[4]R. D. Lawson, P. T. Guenther, and A. B. Smith, Phys. Rev. C **34**, 1599 (1986).
[5]A. B. Smith, P. T. Guenther, and R. D. Lawson, Nucl. Phys. **A483**, 50 (1988).
[6]R. D. Lawson, P. T. Guenther, and A. B. Smith, Phys. Rev. C **36**, 1298 (1987).
[7]R. D. Lawson, P. T. Guenther, and A. B. Smith, Argonne National Laboratory Report No. ANL/NDM-106 (1988); and (unpublished).
[8]J. R. M. Annand, R. W. Finlay, and F. S. Dietrich, Nucl. Phys. **A443**, 249 (1985).
[9]R. W. Finlay, J. R. M. Annand, J. S. Petler, and F. S. Dietrich, Phys. Lett. **155B**, 313 (1985); **157B**, 475 (1985).
[10]D. J. Horen, C. H. Johnson, J. L. Fowler, A. D. MacKellar, and B. Castel, Phys. Rev. C **34**, 429 (1986).
[11]C. H. Johnson and R. R. Winters, Phys. Rev. C **37**, 2340 (1988).
[12]V. Bernard and Nguyen Van Giai, Nucl. Phys. **A327**, 397 (1979).
[13]V. Bernard, Thèse de troisième cycle, Université Paris-Sud, 1978.
[14]G. H. Rawitscher, Nucl. Phys. **A475**, 519 (1987).